A&A 418, 1101–1115 (2004)
DOI: 10.1051/0004-6361:20034332

Astronomy & Astrophysics

A multiwavelength study of solar flare waves

I. Observations and basic properties

A. Warmuth[1], B. Vršnak[2], J. Magdalenić[2], A. Hanslmeier[3], and W. Otruba[4]

[1] Astrophysikalisches Institut Potsdam, An der Sternwarte 16, 14482 Potsdam, Germany
[2] Hvar Observatory, University of Zagreb, Kačićeva 26, 10000 Zagreb, Croatia
[3] Institute for Geophysics, Astrophysics and Meteorology, University of Graz, Universitätsplatz 5, 8010 Graz, Austria
[4] Sonnenobservatorium Kanzelhöhe, 9521 Treffen, Austria

Received 17 September 2003 / Accepted 26 January 2004

Abstract. Propagating wave-like disturbances associated with solar flares – commonly observed in the chromosphere as Moreton waves – have been known for several decades. Recently, the phenomenon has come back into focus prompted by the observation of coronal waves with the *SOHO*/EIT instrument ("EIT waves"). It has been suggested that they represent the anticipated coronal counterpart to Moreton waves, but due to some pronounced differences, this interpretation is still being debated. We study 12 flare wave events in order to determine their physical nature, using Hα, EUV, He I 10 830 Å SXR and radioheliographic data. The flare wave signatures in the various spectral bands are found to lie on closely associated kinematical curves, implying that they are signatures of the same physical disturbance. In all events, and at all wavelengths, the flare waves are decelerating, which explains the apparent "velocity discrepancy" between Moreton and EIT waves which has been reported by various authors. In this paper, the focus of the study is on the morphology, the spatial characteristics and the kinematics of the waves. The characteristics of the common perturbation which causes the wave signatures, as well as the associated type II radio bursts, will be studied in companion Paper II, and a consistent physical interpretation of flare waves will be given.

Key words. shock waves – Sun: flares – Sun: radio radiation – Sun: corona – Sun: chromosphere

1. Introduction

The first indication flare-associated globally traveling disturbances in the low solar atmosphere were given by the activation of distant filaments by flares, first discussed in detail by Dodson (1949; see also Ramsey & Smith 1966). A second line of evidence for propagating agents was provided by the analysis of correlations between flares occurring close in time but at different locations on the solar disk (e.g. Becker 1958; Valniček 1964). However, the reality of this "sympathetic flaring" has remained doubtful until today (for a recent study see Biesecker & Thompson 2000).

In 1960 the existence of flare-associated disturbances was proved by direct optical observations using Hα filtergrams (Moreton 1960; Moreton & Ramsey 1960; Athay & Moreton 1961). The disturbances, which have since become known as *Moreton waves* (a term referring primarily to Hα observations) or – more generally – *flare waves*, appear as arc-shaped fronts propagating away from the flare at speeds of the order of 1000 km s^{-1}. The fronts are seen in emission in the center and in the blue wing of the Hα line, whereas in the red wing they appear in absorption. This behavior was interpreted as a depression of the chromosphere by an invisible agent (Moreton 1964). It was also shown that flare waves can indeed cause the activation or "winking" of filaments (Ramsey & Smith 1966).

Uchida (1968) developed the theory that Moreton waves are just the "ground track" of a flare-produced fast-mode MHD wavefront which is coronal in nature and sweeps over the chromosphere ("sweeping-skirt" hypothesis). In numerical simulations, Uchida (1970; Uchida et al. 1973) was able to show how the waves become focused in regions of low Alfvén velocity, which produced wavefronts that agreed reasonably well with the observations.

Type II solar radio bursts, which are seen in dynamic radio spectra as narrow-band emission drifting from higher to lower frequencies (e.g. Nelson & Melrose 1985), had already been interpreted as the signature of a collisionless fast-mode MHD shock before (Uchida 1960), and it was now comparatively easy to integrate them into the coronal shock scenario (Uchida 1974), especially since it was also observationally shown that they are closely associated with Moreton waves (e.g., Harvey et al. 1974).

Prompted by the study of type II bursts and coronagraphic observations, a debate on the physical cause of propagating shock waves on the sun developed in the 1980s. In the

Send offprint requests to: A. Warmuth,
e-mail: awarmuth@aip.de

classical "blast wave" scenario a flare produces an initial pressure pulse which then propagates through the corona as a fast-mode shock (e.g. Vršnak & Lulić 2000a,b, and references therein), being observed as a Moreton wave in the chromosphere and as a type II burst in the corona. The new hypothesis which was proposed postulated that a CME acts as a piston which generates a driven shock ("piston mechanism"; see Cliver et al. 1999 and references therein). However, this discussion was mainly focused on type II bursts and interplanetary shocks, whereas comparatively little interest was directed towards Moreton waves.

From 1997 onward, globally propagating wave-like features were observed in the low corona (Thompson et al. 1998) with the Extreme Ultraviolet Imaging Telescope (EIT) aboard the Solar and Heliospheric Observatory (*SOHO*) spacecraft. Whether these "EIT waves" are the coronal counterpart to Moreton waves as anticipated by the Uchida model has remained a matter of debate because the two phenomena show several remarkable differences. In particular, EIT waves are on average 2–3 times slower than Moreton waves (Smith & Harvey 1971; Klassen et al. 2000) and are morphologically different.

Several recent studies (Thompson et al. 2000; Warmuth et al. 2001; Khan & Aurass 2002) have shown that at least in certain cases Moreton and EIT waves are closely related and may indeed be regarded as manifestations of the same physical disturbance. In particular, it was shown by Warmuth et al. (2001) that the mentioned velocity discrepancy between Moreton and EIT waves can be straightforwardly explained by the deceleration of the flare waves and several statistical selection effects. In Hα, the waves are observable only during the initial phase of the propagation, when the velocities are still of the order of 1000 km s^{-1}. On the other hand, EIT waves can be traced to much larger distances, but are observed at the low cadence of EIT, so their mean speed is significantly lower (in the order of several 100 km s^{-1}).

Unfortunately, comparative studies of coronal and chromospheric signatures of flare waves are seriously hampered by the low image cadence of EIT (typically 15 min) and problems with EIT timing. Therefore, it is very promising to use data from additional spectral channels. A first step in this direction were soft X-ray observations of coronal flare waves by the Soft X-ray Telescope (SXT) aboard the *Yohkoh* satellite. For one event it has been shown that SXT, EIT and Hα wavefronts are quite consistent and may indeed be caused by the same disturbance (Khan & Aurass 2002). In the same paper, it was shown that there is a fairly good overlapping of the wavefront and the type II burst source observed by the Nançay Radioheliograph (Kerdraon & Delouis 1997). The traces of traveling disturbances were also disclosed in He I 10 830 Å (He I hereafter) filtergrams (Gilbert et al. 2001; Vršnak et al. 2002).

Most of these studies suffer from a small sample of events, and a general lack of multi-wavelength data coverage. The results obtained by Warmuth et al. (2001), for example, were based on only two events, so it might be argued that the conclusions described above may not hold for all Moreton/EIT waves. Indeed, there have been claims that Moreton and EIT waves are distinct phenomena (Eto et al. 2002; Chen et al. 2002).

In order to resolve this question, we study an enlarged sample – 12 flare wave events – and use all available imaging data, including Hα, EUV, He I and SXR images, as well as radioheliograms. This allows us to check the conclusions reached in Warmuth et al. (2001) and derive more convincing and extensive results. In addition, we are now able to provide an overview of the characteristic parameters of flare waves, their ranges and average values.

Our data sources, the principal analysis techniques and a brief description of the data set are given in Sect. 2. Morphological aspects of the waves are described in Sect. 3, while their spatial aspects and their kinematics are discussed in Sects. 4 and 5, respectively. The results are discussed in Sect. 6, and the conclusion is given in Sect. 7.

In the companion paper (Warmuth et al. 2004; henceforth Paper II), the evolution of the perturbation responsible for the creation of flare wave signatures will be studied, and the associated type II radio bursts (which were present in every event) will be analyzed. The outcome of these studies, combined with the results of this paper, will then be used to arrive at a consistent physical interpretation of flare waves.

2. Observations and data set

2.1. Data search

The selection of suitable events started with an inspection of full-disk Hα data. In order to reduce the number of flares that had to be searched, in a first step only those flares which were associated with a metric type II radio burst were considered, since according to Pinter (1977), at least 77% of Moreton waves are associated with type II bursts. To avoid a selection bias, all other flares above a certain importance were also checked for associated Moreton waves.

The data search started with March 1997, when EIT started to operate at cadences that allow the detection of flare waves (Biesecker et al. 2002). The search period covered a total of 54 months (or 4.5 years) and ended in August 2001, which corresponds to the rising and the maximum phase of solar cycle 23.

The full-disk Hα data archives of Kanzelhöhe Solar Observatory (KSO) and Big Bear Solar Observatory (BBSO) were searched according to the scheme described above. Additionally, a thorough search of the Hα data from 1997 to 2000 has been conducted by the staff of Hida Observatory (Shibata et al. 2002), and its results are used here, too. A total of 12 Moreton events were found (KSO: 3; BBSO: 4; Hida: 4; and an additional event observed by B. Reynolds which was first reported in Thompson et al. 2000).

We stress that our only selection criterion was the observation of Moreton wavefronts that were defined clearly enough so that the kinematics of the waves could be measured accurately. This also means that we are studying a sub-category of flare waves, namely those associated with prominent Hα wavefronts. Possibly this represents the high amplitude limit of the phenomenon. In addition, we identified various events that showed some Moreton-like characteristics (i.e. propagating

Table 1. Event overview and data coverage. *Event* gives the event label and date; *NOAA No.* the active region number; *flare loc*. the coordinates of the flare; *flare imp*. the optical and soft X-ray importance of the flare; *SXR beg.-max*. the time of begin and maximum of the SXR flare; $t_{0\,\mathrm{est}}$ the estimated starting time of the disturbance; *1st Moreton* the time of the first Moreton wavefront; and *n* the number of identified wavefronts in the various spectral bands (*Nob*. refers to the Nobeyama radioheliograph). "–" means that no wave features could be detected, and a blank space indicates that no or insufficient data were available.

Event	NOAA No.	Flare loc.	Flare imp.	SXR beg.-max.	$t_{0\,\mathrm{est}}$	1st Moreton	*n* Hα	*n* EIT	*n* He I	*n* SXT	*n* Nob.
E1: 1997 Sep. 24	8088	S31E19	1B/M5.9	02:43–02:48	02:44:00	02:45:00	3	3			8
E2: 1997 Nov. 3	8100	S20W13	SB/C8.6	04:32–04:38	04:35:00	04:36:00	6	2		4	–
E3: 1997 Nov. 3	8100	S20W15	1B/M1.4	09:03–09:10	09:07:30	09:09:10	1	2		2	
E4: 1997 Nov. 4	8100	S14W33	2B/X2.1	05:52–05:58	05:56:00	05:58:00	7	2		–	
E5: 1998 May 2	8210	S15W15	3B/X1.1	13:31–13:42	13:37:49	13:38:57	5	2			
E6: 1998 Aug. 8	8299	N13E74	1B/M3.0	03:12–03:17	03:15:00	03:16:00	5				5
E7: 1998 Aug. 18	8307	N33E87	1B/X4.9	22:10–22:19	22:17:27	22:17:57	7				
E8: 1998 Aug. 19	8307	N33E75	2B/X3.9	21:35–21:45	21:45:33	21:47:54	6		–		
E9: 1998 Aug. 24	8307	N35E09	3B/X1.0	21:50–22:12	22:02:41	22:03:11	9		4		
E10: 2000 Mar. 2	8882	S20W58	SN/M6.5	13:35–13:43	13:38:24	13:39:24	7	2			
E11: 2000 Mar. 3	8882	S15W60	1B/M3.8	02:08–02:14	02:11:30	02:12:00	4	2		–	3
E12: 2000 Nov. 25	9236	N20W23	2B/X1.9	18:33–18:44	18:38:10	18:39:10	8	2	6		

brightenings and winking filaments), but no coherent wavefronts. These events will be discussed in a future paper.

Table 1 gives an overview of the events and the data coverage, introducing the event labels E1 to E12[1]. Note that the flare waves are predominantly associated with active regions (ARs) that produced more than one wave event. This could have important implications for the generation mechanism of the disturbances and will be discussed in a forthcoming paper.

We examine waves seen in five different spectral bands. In all eight events where EIT data were available, EIT waves were really observed, so it is reasonable to assume that all Hα Moreton waves will have associated EIT waves. The association with He I waves and waves seen in the 17 GHz radioheliograms seems to be also quite high (67% and 75%, respectively). Due to the peculiarities in the SXT data acquisition, it is difficult to judge the occurrence rate of the X-ray waves (it is at least 50% in our sample)[2]. These high percentages of association suggest that, generally, all of these different signatures will be present in a flare wave event.

[1] E1 has been discussed in Thompson et al. (2000); E2 in Narukage et al. (2002); E3 in Warmuth et al. (2001) and Khan & Aurass (2002); and E5 in Pohjolainen et al. (2001) and Warmuth et al. (2001). The He I data (E9 and E12) are studied in detail in Vršnak et al. (2002).

[2] The main reason for this is that SXT usually switches automatically to a flare mode, in which primarily partial-frame images are obtained (which might only show a small region and therefore not catch a possible wave) and the exposure time is lowered, so that faint wave features are not recorded (these issues are discussed in detail by Hudson et al. 2003).

2.2. Data sources

Table 2 gives an overview of the imaging instruments used in this study of flare waves. Our emphasis is on Hα (6563 Å) data, which is mainly due to their ready availability and their high temporal cadence (typically 1 min). Data were provided by the KSO Digital Hα Camera (DHC; note that E3 was still recorded on film at KSO), the Singer telescope at BBSO, and the Flare Monitoring Telescope (FMT) at the Hida Observatory of Kyoto University, which provides simultaneous images in Hα line center and both line wings. E1 was observed in the red wing of Hα on film at a cadence of 2−3 min (see Thompson et al. 2000).

Additional chromospheric imaging data in the form of He I 10 830 Å filtergrams were provided by the CHIP instrument at the Mauna Loa Solar Observatory (MLSO). The He I absorption line is formed by the contribution of two distinct processes (see Andretta & Jones 1997 and references therein): the photoionization of helium by coronal UV and EUV radiation and subsequent cascading back (PR mechanism), which is effective in the upper chromosphere, and the direct excitation by collisions from the ground state of parahelium, which dominates at the boundary between the upper chromosphere and the transition region. Therefore, He I filtergrams actually contain information on three different height ranges. While this complicates interpretation, it nevertheless provides us with an interesting link between chromospheric and coronal observations.

As coronal imaging data, we mainly use EUV full-disk images provided by the Extreme Ultraviolet Imaging Telescope (EIT) aboard the *SOHO*. It should be noted that there are

Table 2. Imaging instruments. Spatial resolution is given in arcseconds per pixel, temporal cadence in minutes. Note that the Hida and NoRH data are available at much higher cadences, and that the cadence for SXT applies to each specific combination of filters and exposure times.

Instrument/ Observatory	Wavelength	Spatial resolution	Temporal cadence	Reference	Events
DHC/KSO	Hα	2.3	$\approx$1	Messerotti et al. (1999)	E3, 5, 10
Singer/BBSO	Hα	1.1	0.5–1	Denker et al. (1999)	E7–9, 12
FMT/Hida	Hα, H$\alpha \pm 0.8$ Å	4.2	1	Kurokawa et al. (1995)	E2, 4, 6, 11
CHIP/MLSO	He I 10 830 Å	2.3	3	MacQueen et al. (1998)	E8, 9, 12
EIT/*SOHO*	Fe XII 195 Å	2.6	$\approx$15	Delaboudinière et al. (1995)	E1–5, 10–12
SXT/*Yohkoh*	3–45 Å	4.9/9.8	0.5–2	Tsuneta et al. (1991)	E2–4, 11
NoRH/Nobeyama	17 GHz	10	0.5	Nakajima et al. (1994)	E1, 2, 6, 8

problems with the timing of the EIT images (A. Vourlidas, private communication): the two different methods used to correct erroneous timing give results that may disagree by up to 1 min. We therefore always use the mean of the two corrected times.

A supplementary source of coronal data is the Soft X-ray Telescope (SXT) aboard *Yohkoh*. While the Fe XII images provided by EIT correspond to temperatures of 1.5−1.6 MK, SXT shows plasma at temperatures above 2 MK.

Radioheliograms in the microwave range (17 GHz) were available from the Nobeyama radioheliograph (NoRH). Radio emission at this wavelength arises from both thermal bremsstrahlung and non-thermal gyro-resonance radiation. In the quiet sun, the main contribution is thermal bremsstrahlung from the chromosphere (with a brightness temperature of $T_{\rm B} \approx 10\,000$ K).

2.3. Measurement techniques

We are studying the kinematics of flare waves by utilizing distance-time plots $r(t)$ of their leading edge. To reduce possible sources of error, or at least to get an indication for the accuracy of the derived values, we employ two different measurement techniques. The first is based on the visual determination of the leading edge of the wavefronts. We then determine the distances of the wavefronts from a probable starting location along ten paths which are parts of great circles on the solar surface. They converge in the assumed starting point and reflect the angle into which the wave propagates. Figure 1 shows large-scale Hα images for all events as an overview. Overplotted are the visually determined Hα and EIT wavefronts and the sector in which the measurements were performed.

With the second method, we obtain intensity profiles (using differenced images) along a large number of paths, which are then averaged laterally over the whole sector angle (for details see Vršnak et al. 2002), giving the mean intensity as a function of distance for a given moment. From these profiles we can derive the locations of the leading edge, and compare it with the "visual" values for $r(t)$. Note that the profile method also can provide the location of the intensity maximum and the trailing edge, as well as the evolution of the intensity of the wavefront. These aspects will be discussed in Paper II.

What now remains to be determined is the location of the ignition of the perturbation and its starting time. Usually, the center of the flare is taken as a starting location. This assumption is somewhat arbitrary, therefore, we use the earliest Hα wavefront for an extrapolation of the starting point by fitting a circle to the visually determined leading edge of the front (taking the curvature of the surface into account). This is not an exact method (e.g., the central parts of the perturbation could be slightly faster than those at the periphery, leading to an elliptical shape of the front), but it makes no assumptions about the initiation of the perturbation, in contrast to the usual "flare center" approach.

The estimated starting time ($t_{0\,\rm est}$) was usually taken as the time of the last Hα image without a visible wavefront in all events where the Hα cadence was 1 min or better. In several cases, the time of the impulsive rise of the microwave burst and the evolution of the Hα flare (the presence of ejecta or a sudden expansion of the flaring area) were used to derive $t_{0\,\rm est}$. Note that our study of the kinematics does not depend on the exact starting times. A perhaps more objective estimation of the probable starting times will be presented in Sect. 5.1.

3. Morphology

3.1. Hα

In Fig. 2, the morphology and evolution of the Moreton wave of E5 (which is the best-observed event in Hα) is shown in Hα difference images. We note that the Moreton wavefronts in fact consist of two distinct features: a diffuse arc of more or less homogeneously increased emission, and a number of small discrete brightenings. The wavefronts are not observed in the immediate vicinity of the flare, but make their first appearance at a considerable distance from the flare and the starting point.

As the wave propagates away from the flare, the diffuse front becomes progressively less intense and also less homogeneous, while its thickness Δr increases. As the diffuse front travels over the surface, the localized brightenings light up and then slowly fade over a period of several minutes, which means that they still can be discerned after the diffuse wavefront has

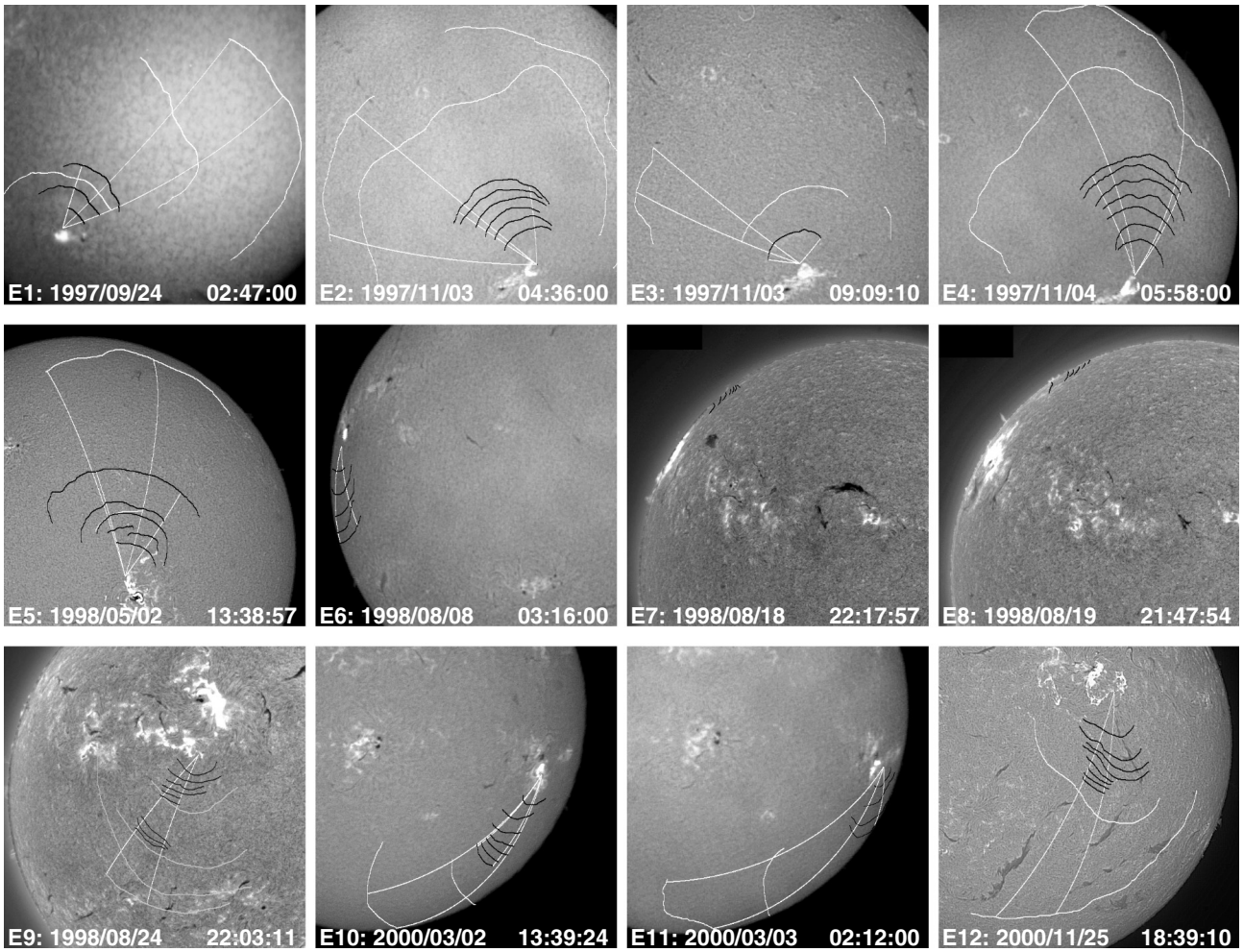

Fig. 1. Overview of the Moreton and EIT waves of E1 to E12. The visually determined Hα (black) and EIT wavefronts (white) are plotted on Hα images from the time of the wave onset (for E9, the He I fronts are shown instead of EIT). Also shown are parts of great circles which define the sectors in which the distances of the wavefronts from the calculated starting point were measured (for the cases where Hα and EIT waves were measured using different sectors, both of them are shown). In this and all subsequent images, solar north is up, west is right, and times are given in UT.

passed over them. As the wave propagates farther, the newly activated localized brightenings become progressively fainter and more diffuse. Before the signatures of the disturbance become too faint to be distinguished from the background, the wavefront has turned into an inhomogeneous ensemble of small brightenings with some very faint remnants of the diffuse front.

We emphasize that some of the localized brightenings light up even before the wavefront has reached them. The distance to the leading edge can range up to 25 Mm. This indicates that there is some agent that can influence regions in the chromosphere before the wavefront itself is actually passing over.

In the wings of Hα, the overall morphology of the wavefronts is the same as in the line center, and the waves seen in the three spectral bands are also roughly cospatial. In the blue wing (Hα_b hereafter), the fronts are seen in emission, while they appear as dark absorption features in the red wing (Hα_r). In all cases, the contrast of the wavefronts is higher in the wings than in the line center, especially in Hα_r. There, the absorption wavefronts are followed by an emission feature of a larger thickness Δr and a lower contrast. In Hα_b, similar trailing disturbances are observed seen in absorption.

In all events the excess emission clearly arises from an enhancement of pre-existing chromospheric structures, and not from matter propagating above the surface (e.g. Hα sprays).

3.2. EIT

EIT waves show a wide range of morphological patterns (cf. Klassen et al. 2000). Usually they are observed as diffuse and irregular arcs of increased coronal emission, but about 7% of them display sharp and bright wavefronts – the so-called S-waves (Biesecker et al. 2002). Most of these events show also the more common diffuse fronts in a later stage of the event, and it is reasonable to suppose that the initially sharp fronts decay to the diffuse fronts in the course of their propagation (as is observed in the case of Moreton waves).

In two of the eight events that had EIT coverage – E1 and E5 – such S-waves were found, and in both events the following EIT images showed the more usual diffuse fronts.

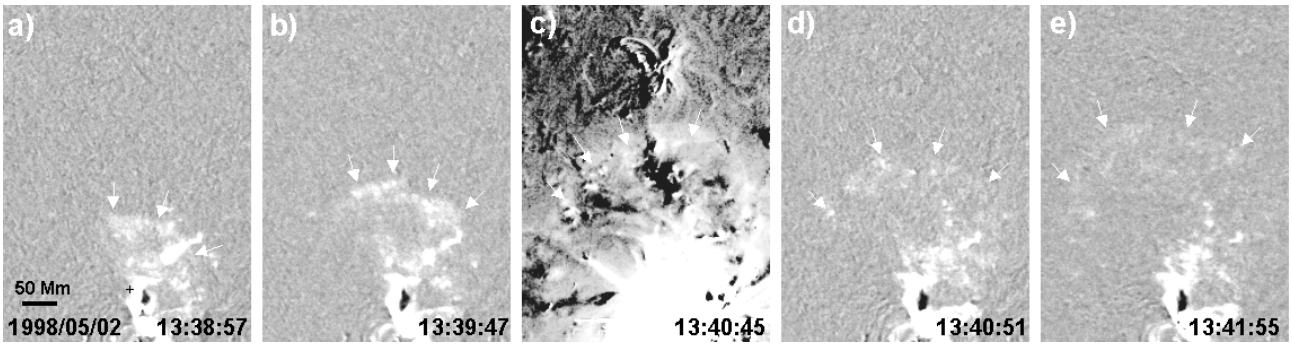

Fig. 2. Evolution of the flare wave of 1998 May 2 (E5) as shown by Hα **a)**, **b)**, **d)**, **e)** and EIT **c)** difference images. The wavefronts are indicated by arrows.

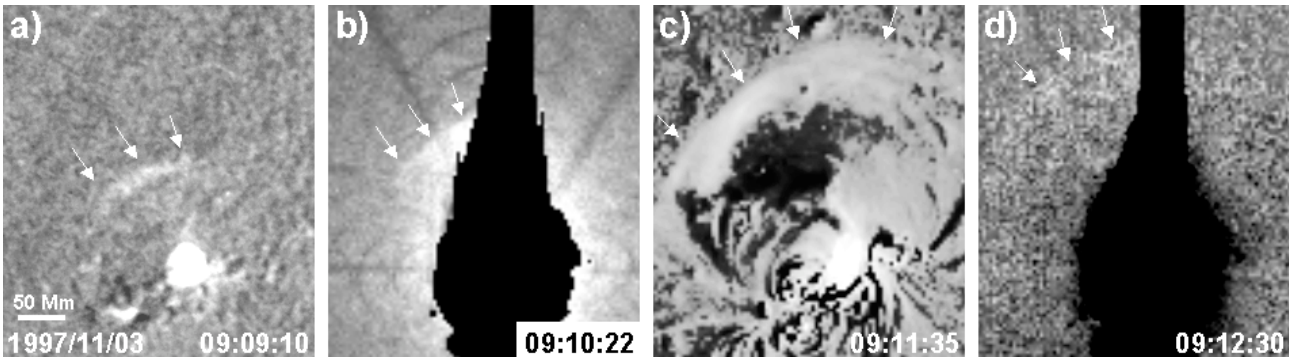

Fig. 3. The flare wave of 1997 November 3 (E3) as shown by Hα **a)**, SXT **b)**, **d)** and EIT **c)** difference images. The black features in the SXT images are artifacts of saturation.

Those two events were also the only ones where an EIT wavefront could be observed within the spatial and temporal range of the Hα Moreton fronts, and they offer a unique opportunity to compare the morphology and the exact location of EIT and Moreton fronts.

In E1, the EIT front is very thin ($\Delta r \approx 20$ Mm) and has a sharp leading edge. Behind the front discrete patches of increased emission are visible. The corresponding Hα front (observed in Hα_r) has a roughly similar overall shape and angular extent. In the case of E5 (Fig. 2), the S-wave is mainly visible due to localized brightenings that map a continuous front. There is probably also a diffuse part of the wave, but this is obscured by scattered light from the flare. Many of the distinct brightenings correspond remarkably well with the features seen in Hα, and also the overall shape and angular extent of the wavefronts agree nicely. This supports the hypothesis that Hα and EIT waves are signatures of the same physical disturbance.

The first EIT front in E3 (see Fig. 3c) was also an exception: while it was not as thin as the S-waves ($\Delta r = 30$–80 Mm), it was very bright and had a well defined leading edge. In the other five events with EIT data coverage, only the conventional diffuse EIT fronts were seen. This is probably due to the low image cadence of EIT, since all of these fronts were observed already at large distances ($r > 300$ Mm).

In general, there is a large range in relative intensity change within the fronts (as obtained by applying the "profile method" to the EIT images and taking the difference of consecutive profiles). The brightness increase averaged over the whole wavefront ranges from more than 60% (the S-wave of E1) down to below 10% (see also the discussion of the EIT intensity profiles in Paper II, Sect. 3.4). Several wavefronts (especially for $r > 600$ Mm) were so faint that the brightness increase could not be measured by integrating over the front. These wavefronts were only marked by several smaller brightenings mapping out an arc, which allowed the determination of the leading edge only with the "visual" method.

EIT waves, like Moreton waves, tend to avoid concentrations of magnetic fields, such as ARs and polar coronal holes. This is nicely shown by E3, where the wavefront splits into two parts before encountering a small AR in the northern hemisphere. The influence of magnetic structures on the wave propagation also explains the fact that the EIT fronts that are far from the flaring AR generally have an irregular shape, while the curvature of the fronts that are observed near the wave origin agrees rather well with a circular segment (cf. Fig. 1 and Sect. 4.1).

EIT waves can extend over a significant height range in the low corona. This is demonstrated by EIT waves that are observed at the solar limb, e.g. in E10 and E11, where the wavefront was observable up to heights of more than 100 Mm (see also the EIT wave in Hudson et al. 2003). EIT waves that are propagating on the disk are therefore observed as the integration along the line of sight, projected onto the plane of sky. This means that the apparent leading edge that is used to measure the kinematics of the wave may not be identical to the "true" leading edge of the wave at the height of the intersection between chromosphere and corona. Nevertheless, since the majority of the emission increase occurs relatively close to the surface, no

dramatic mismatches are expected. Indeed, the nearly cotemporal Hα and EIT wavefronts in E1 and E5 are cospatial to within ±20 Mm.

A discussion of the morphology of EIT waves would not be complete without mentioning coronal dimming (see, e.g., Khan & Hudson 2000; Gopalswamy & Thompson 2000; Thompson et al. 2000). All EIT waves were associated with pronounced EUV dimming, which is observed as a sudden significant decrease of emission behind the EIT wavefronts. Initially, the dimming area is a rather compact region partially covering the space between the flaring AR and the EIT front (see, e.g. Figs. 2c and 3c). As the EIT wave expands, so does the dimming area behind it, though the area of significant dimming must not necessarily expand with the wavefront during its whole propagation. The dimming areas are rather inhomogeneous (smaller patches within them may even show no dimming at all), they lack sharp borders, and their average intensity relative to the emission of the quiet corona (measured by applying the "profile method" to the EIT frames) spans from 95% down to 65%, with a mean of 85%. The dimming areas remain stationary long after the EIT waves have vanished, and slowly return to their pre-event brightness on a timescale of several hours.

Dimming is often associated with CMEs (e.g. Harrison et al. 2003), and indeed CMEs were detected in practically all events: no coronagraphic observations were available for E6, E7 and E9, but the observations of interplanetary type II bursts strongly suggest the presence of CMEs in E7 and E9, which leave E6 as the only event without any indication of a CME. Therefore, dimming may primarily be a result of the CME, and not of the flare waves. A closer examination of the wave-CME relation will be carried out in a forthcoming paper.

3.3. Helium I

Figure 4 shows the He I wave of E9. The He I wave can be seen as an expanding broad arc-shaped front of increased absorption. The dark front has a much larger thickness Δr than the corresponding Hα front, it is inhomogeneous and lacks a sharp edge. It consists of an extended diffuse component and a number of discrete darker patches. These patches coincide with the He I mottles that reproduce the chromospheric network, and with the photospheric magnetic field. Thus, the patchy features in the wavefront are caused by the increased absorption in magnetic field concentrations (see Vršnak et al. 2002).

Some regions behind the He I front show a weakening of absorption, morphologically reminiscent of the coronal dimming observed behind EIT waves. In E12, a comparison with the contemporaneous EIT images shows that at the locations where the dimming is strong in EIT, the He I absorption tends to be reduced with respect to the pre-event state, although there is no one-to-one correspondence (Vršnak et al. 2002).

3.4. SXT

The two X-ray wavefronts that were observed in E3 are shown in Fig. 3. They appear as homogeneous emission with a sharp leading edge. Their overall shape and azimuthal extent agrees closely with the single observed Moreton wavefront, and to a somewhat lesser extent with the first EIT wavefront. The thickness Δr of the X-ray wave could not be determined in this event since its trailing edge is obscured by scattered light from the flare.

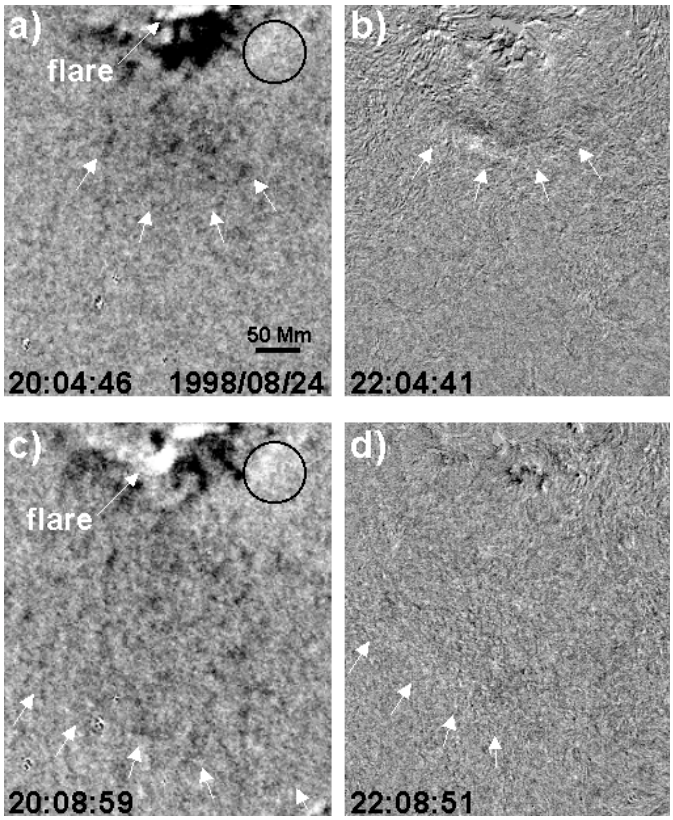

Fig. 4. The flare wave of 1998 August 24 (E9) as shown by He I difference images **a)**, **c)** and Hα running difference images **b)**, **d)**. The black circle in **a)** and **c)** indicates an area of decreased He I absorption.

The X-ray wave in E2 (see Narukage et al. 2002) is very faint and therefore not well suited for morphological studies. However, we note that its overall shape and azimuthal extent again agrees reasonably well with the Moreton wave. In E11, an arc-shaped propagating feature was detected, but since it has fixed footpoints, it is probably an erupting loop and not a wave.

3.5. 17 GHz radioheliograms

A morphological study of flare wave signatures from radioheliograms is complicated by the fact that many artifacts are present in the images (due to the image synthesis algorithms) which must not be confused with real features. Therefore, the analysis will be restricted to the global appearance of the waves.

As an example, 17 GHz radioheliograms (in differenced form) are presented in Fig. 5 for E6. The wave is seen in emission and roughly resembles the accompanying Moreton wave in shape and angular extent. However, it is more diffuse (which is at least partly due to the limited resolution of the radioheliographic data) and has a much larger thickness Δr

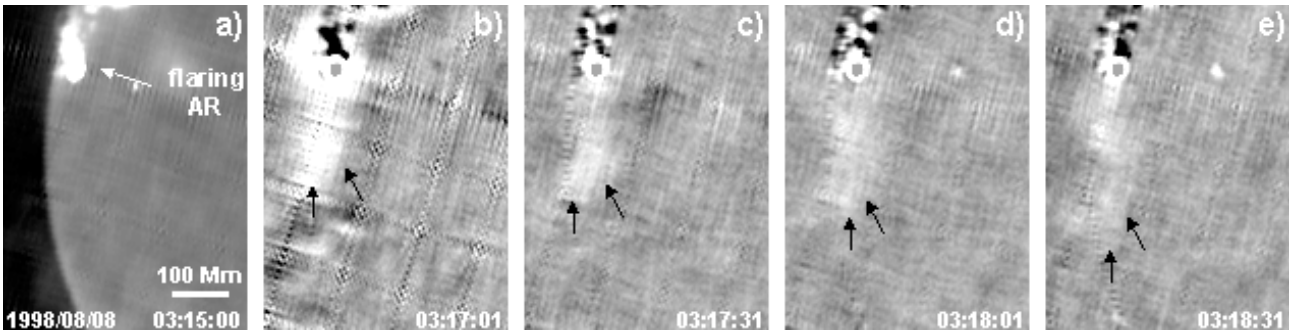

Fig. 5. The flare wave of 1998 August 8 (E6) as shown by 17 GHz difference images **b)–e)**. **a)** is a pre-event direct radioheliogram showing the flaring active region and the undisturbed chromosphere.

(up to 170 Mm). In the limb events of E6 and E11, the excess emission does not extend beyond the limb, which means that in this respect the waves resemble more closely Moreton waves than EIT or X-ray waves.

Since the primary contribution in the 17 GHz range is thermal emission from the chromosphere and transition region, the wave signature is probably due to the compression and/or heating of these layers. In E6, the brightness temperatures T_B can be estimated: in the quiet chromosphere T_B was about 10 000 K, while the maximum brightness temperature in the first clearly visible wavefront (03:17:01) was $T_B \approx 13\,500$ K.

4. Spatial characteristics

4.1. Wavefront shape

The leading edges of the earliest wavefronts (as determined with the "visual" method) agree very closely with a circular curvature. Figure 6 shows the deprojected leading edges of the first Hα wavefronts (excluding the limb events E6 to E8), together with the fitted circles (the center of the circles was used as the extrapolated wave source point). We have calculated a simple error estimate by measuring the mean absolute deviation between the actual front and the fitted circle, averaged across the whole wavefront angle, and normalized by the radius of the circle, $\langle \Delta r \rangle / r_c$. Excluding the limb events, where projection effects tend to increase the fitting errors, $\langle \Delta r \rangle / r_c$ lies between 0.01 and 0.02 for the first Moreton wavefronts. An exception is E12 with $\langle \Delta r \rangle / r_c = 0.35$. From Fig. 1, it is evident that E12 was the most irregular wave event. This may be due to the influence of the filament which can be seen lying in the middle of the wave's path.

With increasing distance, the leading edges of the wavefronts become more irregular (see Fig. 1), but generally, they retain a basic circular curvature – in many events, $\langle \Delta r \rangle / r_c$ does not increase significantly. The first EIT wavefronts in E1, E3 and E5, as well as the first He I front in E9, also agree nicely with a circle ($\langle \Delta r \rangle / r_c = 0.01$–$0.025$; see Fig. 6), whereas the EIT fronts which are farther from the flaring AR (say, $r > 300$ Mm) show larger deviations from a circular shape ($\langle \Delta r \rangle / r_c \approx 0.05$–$0.10$). Still, the retention of a basic circular curvature over large distances is a strong indication of the wave-like nature of the disturbances.

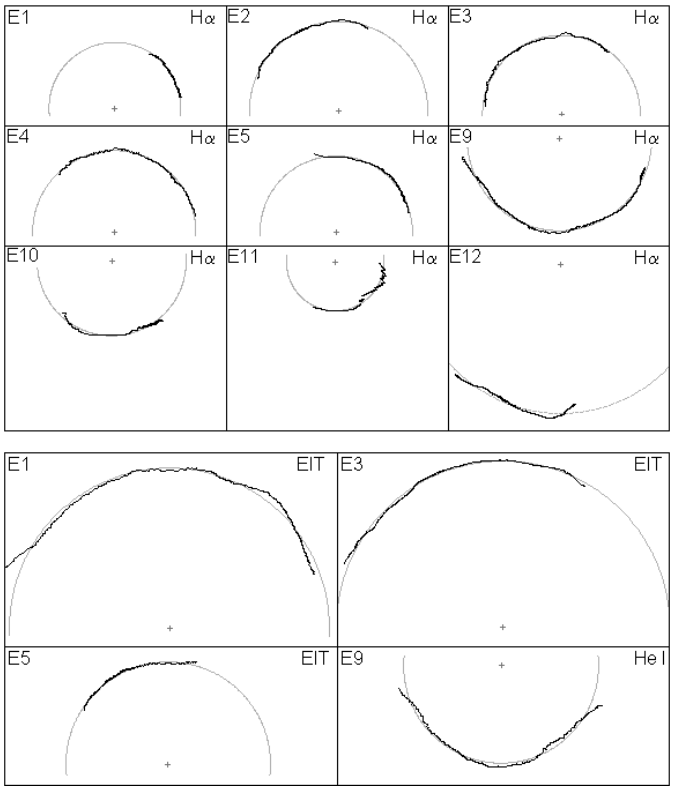

Fig. 6. *Upper part:* deprojected leading edges of the first observed Hα wavefronts (*black*), shown together with a circular fit (*grey*). *Lower part:* deprojected leading edges of the first EIT wavefronts in E1, E3, and E5, and of the first He I wavefront in E9. In all plots, solar north is up. The individual plots are not shown to scale.

4.2. Angular extent

In most events, the angular extent of the wavefronts changes with time/distance. Therefore, an initial angular width ϕ_0 is defined, which is the angle that the first wavefront spans, and an average propagation width $\bar{\phi}$, which determines the angle within which the kinematics of the wave is measured ($\bar{\phi}$ is the angle depicted in Fig. 1).

The angle ϕ_0 ranged from 56° to 150° (excluding the extreme limb events), with a mean of 99°, while $\bar{\phi}$ fell in the range between 15° and 62°, with a mean value of 40°. These values agree reasonably well with the mean Moreton angular width

of 84° found by Smith & Harvey (1971), who did not make the distinction between initial and average angle.

In all events ϕ_0 is larger than $\bar{\phi}$, which is due to two different reasons: since $\bar{\phi}$ is the arc that *all* wavefronts have to cover, a single badly visible front (where only the central parts of the front could be identified) can significantly reduce $\bar{\phi}$, although the other fronts have a consistently large angular width. On the other hand, in some events (e. g. E9 and E12) there seems to be a real physical reason behind $\phi_0 > \bar{\phi}$, because the later wavefronts really display a systematically smaller ϕ.

Due to their much more irregular shape, it is difficult to define the propagation angles for EIT waves, especially since the second EIT fronts are usually too ill-defined. It is more reasonable to compare the angular extents of the first EIT fronts to the Moreton fronts in the three events where the EIT wave was observed near the flaring AR. While the wavefronts in E3 and E5 agree in angular extent, in E1 the EIT front was significantly more extended.

In E9, the only event where a direct comparison of Hα and He I wavefronts was possible, the initial angle ϕ_0 of the He I front was 115°, whereas in Hα it was 150°. However, while the Moreton wave experienced very strong shrinking ($\bar{\phi} = 21°$), the He I wave remained comparatively broad ($\bar{\phi} = 51°$).

The X-ray waves had similar angular extents as the accompanying Hα waves and did not show signs of shrinking. The wavefronts seen in the radioheliograms were too diffuse and noisy to allow a quantitative definition of the propagation angle, but they were broadly similar to the Moreton waves.

4.3. Starting location

In all nine cases where the starting location could be determined (excluding the limb events E6, E7 and E8), the calculated origin of the wave was lying in the periphery of the flaring AR, clearly displaced from the central parts of the flare (see Fig. 1). The distance between the starting point and the center of the Hα flare amounted to 25−164 Mm, with a mean of 58 Mm. The two largest offsets (in E9 and E12) could be accounted for by the fact that the wavefronts were centered on remote flare brightenings of weaker intensity that might be responsible for the wave launch. However, even when we exclude E9 and E12, the mean value for the displacement from the flare center is 40 Mm.

It might be argued that the calculated starting points do not really represent the true wave origins. In E1, E3 and E5, both the Hα and the first EIT wavefronts are defined clearly enough so that they can be used to extrapolate starting points independently. The same is true for the X-ray wave in E3 and the He I wave in E9. The various calculated origins differ on average by about 40 Mm. If we assume that all different signatures originate from the same location, this in a way defines the accuracy of the extrapolation method. The measured offsets of the starting locations from the associated flares are of about this value, but since the calculated sources are *systematically* displaced in the direction away from the flare, the offsets have to be considered as real. Furthermore, Khan & Aurass (2002) and Hudson et al. (2003) also found these offsets using a totally different extrapolation technique.

5. Kinematics

5.1. Hα

In Fig. 7 the distance r of the leading edge of the Hα wavefronts from the calculated source point is shown as a function of time t for all studied events except E3, where only a single Moreton wavefront was detected. In all subsequent figures, the zero time $t = 0$ corresponds to the estimated starting time $t_{0\,\mathrm{est}}$ of the disturbances. Overplotted are 2nd degree polynomial fits and power-law fits of the form

$$r(t) = c\,(t - t_{0\,\mathrm{pl}})^{\delta} \tag{1}$$

where δ is the power-law exponent, $t_{0\,\mathrm{pl}}$ the starting time given by the fit (t at $r = 0$), and c is a constant.

Figure 8 shows the velocities v derived from the consecutive wavefront pairs. The rather large scatter in some of the v data points is due to two causes. Firstly, errors in the determination of the leading edge are amplified since each velocity is derived from a wavefront pair. Secondly, the propagation of the wavefronts often becomes inclined with respect to the great circles along which $r(t)$ is measured, which leads to an increase in the range of measured velocities.

From the plots in Figs. 7 and 8, it is evident that all Moreton waves experience significant deceleration during their propagation. Table 3 shows the kinematical parameters for all events, measured using the "visual" method. In E1, E2, E4, E6 and E12, images taken in Hα_r were used for deriving the kinematical parameters since the waves have the highest contrast in this spectral band. Table 3 includes the measured first and last velocities v_1 and v_l (derived from the first and the last wavefront pair), the velocity $v_{0\,\mathrm{est}}$ obtained from the 2nd degree polynomial fit at $t = t_{0\,\mathrm{est}}$, the mean velocity $\bar{v}$ derived from a linear fit of $r(t)$, the minimum and maximum distances $r_{\min}$ and $r_{\max}$ of the wavefronts, the average deceleration $\bar{a}$ derived from the polynomial fits, and finally the power-law exponent δ.

In the last four rows of Table 3 the results are summarized by displaying the mean values and standard deviations of all parameters for the visual and the profile method, respectively (the "profile-method" values for the individual events are not shown in the table). The summary shows that the kinematical parameters derived by the two different measurement techniques (note that the average "profile" values do not include E1 due to the lack of a suitable pre-event image) are generally in a good agreement, and some of them agree exceptionally well, e.g. $\bar{v}$.

The good correspondence between the mean kinematical values given by the visual and the profile method proves that both schemes generally reproduce the true kinematics of the Moreton waves well. However, it seems that usually the visual method is more accurate in determining the leading edge of the disturbances, and henceforth we will refer only to the "visual" parameters in our discussion.

The first measured velocities v_1 have a mean of $\langle v_1 \rangle = 845 \pm 162$ km s^{-1}. The mean of the average velocities amounts

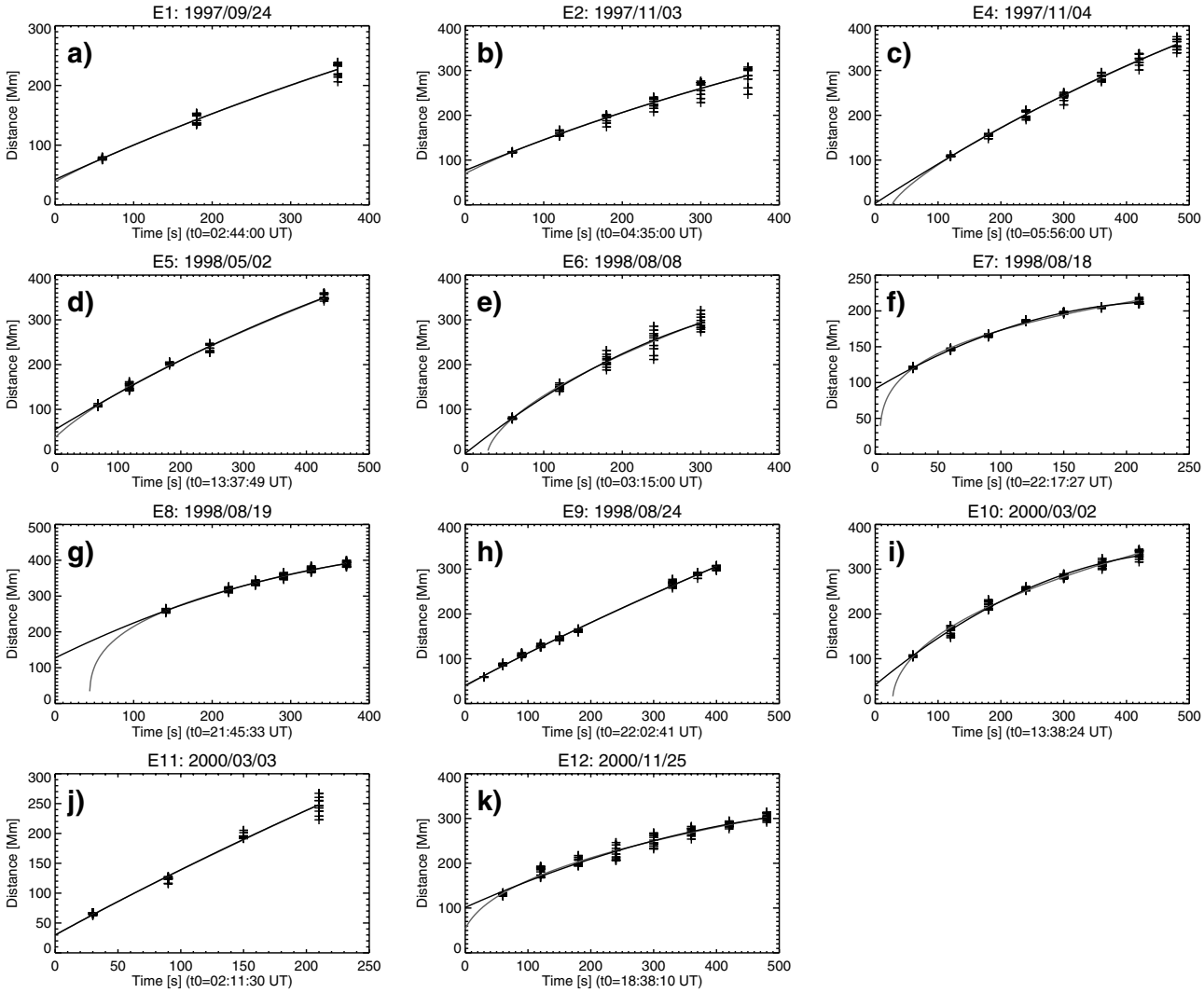

Fig. 7. The kinematics of the leading edges of the Moreton waves (visually determined from Hα difference images) of the events E1 to E12 (excluding E3, where only one wavefront was observed). The distances $r(t)$ (*crosses*) are plotted together with 2nd degree polynomial least-squares fits (*thick line*) and power-law fits (*thin line*). The time t is counted from the estimated starting time $t_{0\,\mathrm{est}}$ ($t0$ in these plots). Distances are given in Mm (10^3 km).

to $\langle \bar{v} \rangle = 643 \pm 179$ km s^{-1}, which agrees very closely with the value of 658 ± 159 km s^{-1} found by Smith & Harvey (1971). Evidently, Smith & Harvey were using linear fits and did not detect the deceleration.

The average decelerations $\bar{a}$ have a much larger scatter than the velocities, with a mean of $\langle \bar{a} \rangle = -1495 \pm 1262$ m s^{-2}. The waves do not display a constant deceleration, instead, the deceleration tends to become weaker with increasing time and distance. For example, if only the first three fronts are used to derive the polynomial fits, then the mean of all decelerations is significantly larger at $\langle \bar{a} \rangle = -2460$ m s^{-2}. Consequently, the kinematical paths of the wavefronts are represented better by the power-law fits. This is also evident from the calculated exponent δ, which has a smaller scatter than $\bar{a}$: its average over all events was $\langle \delta \rangle = 0.62 \pm 0.22$.

The Moreton waves could be tracked out to $\langle r^{\max}_{\mathrm{H}\alpha} \rangle = 301 \pm 47$ Mm, and were first observed at a distance of $\langle r^{\min}_{\mathrm{H}\alpha} \rangle = 97 \pm 26$ Mm (these averages exclude the events where the starting location could not be back-extrapolated, and also E3, which had a low image cadence in Hα).

Interestingly, the extrapolated wavefront distance r_0 at the starting time $t_{0\,\mathrm{est}}$ (not shown in Table 3) is rather large with a mean of $\langle r_0 \rangle = 49 \pm 30$ Mm. This means that either the waves are starting from a location significantly farther out, the assumed starting times are too late, or the disturbances are initially significantly faster and suffer a strong initial deceleration. The first possibility is unlikely since the extrapolation method is too accurate to account for such large mismatches. Conversely, it might well be that the disturbances are only visible in Hα after they have steepened sufficiently. The waves would have already been launched at $t_{0\,\mathrm{est}}$, but would only be detected on a later Hα image. If that is the case, we can adopt a new starting time $t_{0\,\mathrm{poly}}$, which is the time at which the polynomial fit of $r(t)$ reaches $r = 0$.

On the other hand, we have seen that the power-law fits seem to represent the kinematics of the waves better, and they

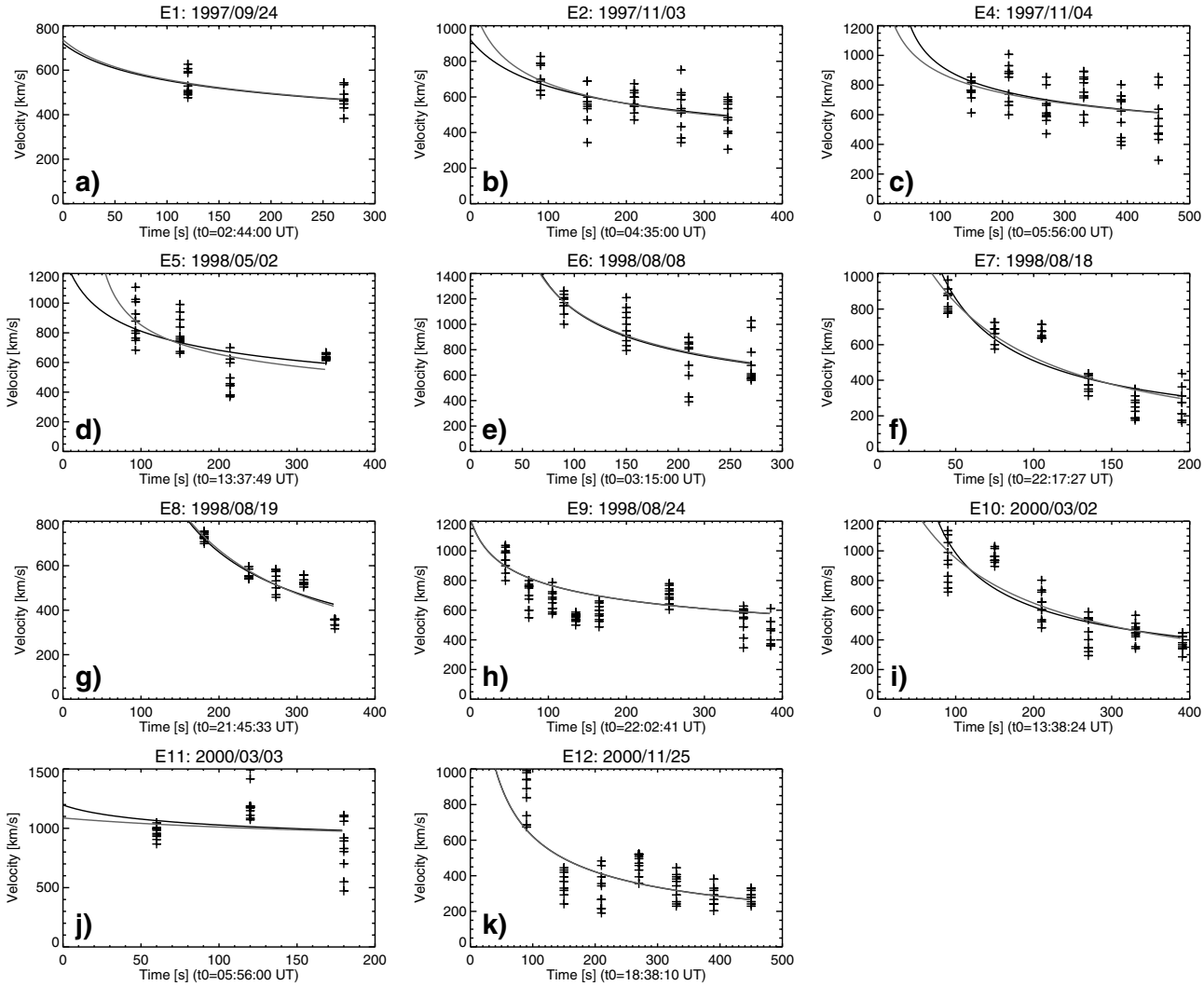

Fig. 8. The velocities $v(t)$ (*crosses*) derived from consecutive Moreton wavefront pairs of events E1 to E12 (excluding E3). Also shown is the derivative of the power-law fits of $r(t)$ (*thick line*) and a 2nd degree polynomial fit of $v(t)$ (*thin line*). Velocities are given in km s^{-1}.

yield higher initial deceleration, which would reduce r_0. An even stronger initial deceleration than the one predicted by the power-law fits may be caused by the denser medium close to the AR.

From the available data, it is not possible to determine which of the two effects is dominating, and therefore the "true" launch time of the disturbances cannot be derived. However, for our present purposes, we have no need of more accurate starting times. Generally, $t_{0\,\mathrm{est}}$ and $t_{0\,\mathrm{pl}}$ were in rough agreement (to ±30 s), while $t_{0\,\mathrm{poly}}$ was systematically earlier by ≈1 min.

5.2. EIT

In Fig. 9 the distances $r(t)$ for the observed EIT wavefronts are plotted together with the distances of the Hα fronts for all events with EIT coverage, and for E9 (Fig. 9f), for which He I instead of EIT wavefronts are plotted. Also shown are 2nd degree polynomial fits and power-law fits applied to the combinations of Hα and EIT $r(t)$ data points. If Moreton waves and EIT waves are signatures of the same physical disturbance, they should lie on closely associated kinematical curves. Indeed, Fig. 9 shows that in most events EIT and Hα wavefronts agree quite well with the fitted curves. The agreement is best in E1 and E5, and worst in E10, which might be due to the poor Hα data quality in that event.

In Table 4 the kinematical properties of the EIT waves are listed, as well as the parameters derived from the combined EIT and Hα data (denoted by the suffix *cb*). This includes the mean EIT velocities $\bar{v}_{\mathrm{EIT}}$, the minimum and maximum EIT distances $r_{\mathrm{EIT}}^{\mathrm{min}}$ and $r_{\mathrm{EIT}}^{\mathrm{max}}$, the mean combined velocities $\bar{v}_{cb}$, the mean combined decelerations $\bar{a}_{cb}$, and the exponent δ_{cb} of the power-law fits of the combined data.

The EIT wave velocities $\bar{v}_{\mathrm{EIT}}$ are significantly lower than the Hα speeds. The mean value is $\langle \bar{v}_{\mathrm{EIT}} \rangle = 311 \pm 84$ km s^{-1}. In all events, the fits of the combined Hα and EIT data show significant decelerations, and $\bar{a}_{cb}$ is smaller (i.e. less negative) than $\bar{a}_{\mathrm{H}\alpha}$ in every case. This is a consequence of the decrease of the deceleration with increasing time and distance.

The power-law exponent is $\langle \delta_{cb} \rangle = 0.63 \pm 0.1$ for the combined data. When only the seven events that have EIT data coverage and more than one Moreton wavefront are considered, so that the same events are included in averaging, then

Table 3. Hα Moreton wave kinematics derived with the "visual" method. v_1 and v_l are the measured first and last velocities, $v_{0\,\mathrm{est}}$ the velocity obtained from the polynomial fit of $r(t)$ at the estimated starting time, $\bar{v}$ the mean velocity derived from a linear fit, $r_{\min}$ and $r_{\max}$ the minimum and maximum distances of the wavefronts, $\bar{a}$ the average deceleration derived from the polynomial fits, and δ is the exponent of the power-law fits. The last four rows give the mean values and standard deviations σ of the parameters obtained by the "visual" and the "profile method", respectively. Values in brackets are inaccurate and are not used for deriving the mean values. Decelerations are given in m s^{-2}, velocities in km s^{-1}, and distances in Mm (10^3 km).

Event	v_1	$v_{0\,\mathrm{est}}$	v_l	$\bar{v}$	$r_{\min}$	$r_{\max}$	$\bar{a}$	δ
E1	542	600	469	496	78	227	−484	0.78
E2	709	719	491	568	118	289	−718	0.69
E4	762	914	553	695	109	357	−730	0.76
E5	875	847	637	659	108	350	−744	0.71
E6	1 164	1 398	695	884	(80)	(294)	−2 856	0.61
E7	847	1 040	260	507	(121)	(213)	−4 442	0.29
E8	729	1 074	350	572	(259)	(390)	−1 966	0.34
E9	946	740	446	655	59	303	−382	0.88
E10	922	1 156	381	619	106	333	−2 234	0.47
E11	963	1 144	843	1024	66	246	−1 000	0.91
E12	836	629	285	390	131	303	−886	0.41
Mean (vis):	845	933	492	643	97	301	−1 495	0.62
σ (vis):	162	252	179	179	26	47	1 262	0.22
Mean (prof):	813	942	545	647	106	278	−1 794	0.57
σ (prof):	192	217	159	155	36	77	1 136	0.2

$\langle\delta_{cb}\rangle = 0.64\pm0.1$ and $\langle\delta_{\mathrm{H}\alpha}\rangle = 0.68\pm0.18$. This close agreement of $\delta_{\mathrm{H}\alpha}$ and δ_{cb} once more shows that Moreton and EIT waves are following kinematical curves that are closely associated.

The EIT wave of E1 was the only one where three wavefronts could be identified, and a deceleration of $\bar{a}_{\mathrm{EIT}} = -105$ m s^{-2} could be derived. As a comparison, for the EIT waves of 1997 April 7 (Thompson et al. 1999) and 1997 May 12 (Thompson et al. 1998), decelerations were found of -242 m s^{-2} and -62 m s^{-2} (derived from the first three fronts), respectively. This shows that deceleration is also detectable in EIT wave events that are not associated with Hα signatures.

The mean minimum and maximum observed distances of the EIT fronts were $\langle r^{\min}_{\mathrm{EIT}}\rangle = 390 \pm 183$ Mm and $\langle r^{\max}_{\mathrm{EIT}}\rangle = 785 \pm 126$ Mm, which are both significantly larger than the corresponding values for the Moreton waves. Comparison of the values of $r_{\max}$ clearly shows that EIT waves can be traced to much larger distances than Moreton waves. On the other hand, the large $r^{\min}_{\mathrm{EIT}}$ are the consequence of the low image cadence of EIT.

5.3. Helium I

In Fig. 9f, $r(t)$ of the He I and the Hα fronts is plotted for E9 (in Fig. 9i, the He I fronts determined with the "profile" method are shown for E12, but the plot is quite crowded). Again the deceleration is evident. The He I and Hα perturbations are obviously related since they follow closely associated kinematical curves. Yet the He I fronts are leading the Hα fronts by about 30 Mm. The same was found for E12. This behavior was interpreted by Vršnak et al. (2002) in terms of a signal which reaches the chromosphere before the actual shock arrival, and we will return to discuss it in Paper II.

The He I velocities (e.g., E9: $v_{1\,\mathrm{He}} = 610$ km s^{-1}) as well as the deceleration $\bar{a}_{\mathrm{He}}$ lie in between the usual values for Hα and EIT waves. This is due to the fact that the He I wavefronts are observed both close to the flaring AR (a consequence of the 3 min cadence of the He I filtergrams) and at large distances where Hα waves are no longer detectable (E9: $r^{\max}_{\mathrm{He}} = 493$ Mm, $r^{\max}_{\mathrm{H}\alpha} = 303$ Mm). In that way, the He I disturbances may be regarded as a "missing link" between Moreton and EIT waves.

5.4. SXT

In E2, the X-ray fronts were very dim and diffuse, and no detailed analysis was performed. However, the kinematics of the X-ray wave is reported by Narukage et al. (2002), who found an average speed of $\bar{v}_{\mathrm{X}} = 630 \pm 100$ km s^{-1}. The X-ray wavefronts were found to lead the Moreton fronts by ≈10–20 Mm.

The two X-ray wavefronts of E3 yield a speed of $v_{\mathrm{X}} = 595$ km s^{-1}. Figure 9c shows that the two X-ray fronts, the single Hα front, and the first EIT front give a remarkably consistent kinematical picture. An average deceleration of $\bar{a} = -227$ m s^{-2} is found for the combined data.

In both events, the maximum distance at which the X-ray wave was observable was ≈200 Mm, which is less than $r^{\max}_{\mathrm{H}\alpha}$.

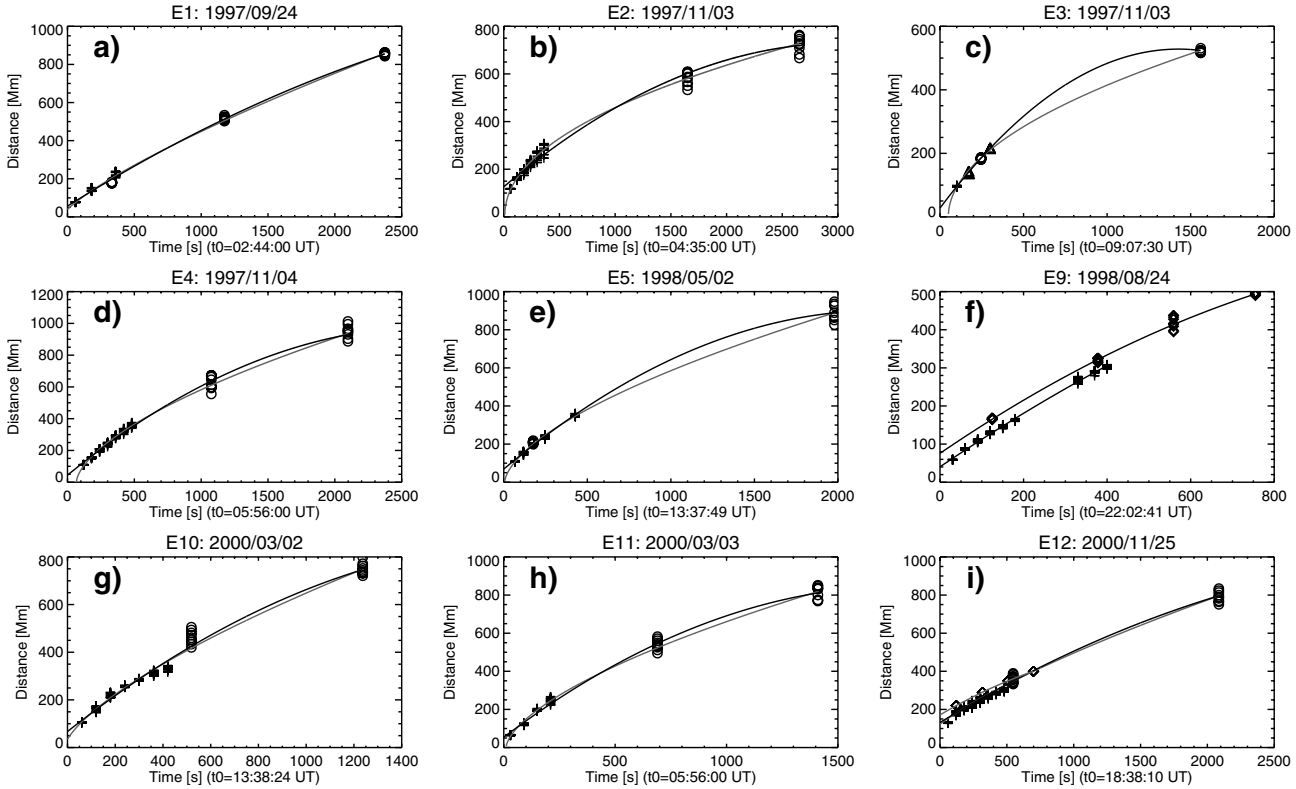

Fig. 9. The combined kinematics of the Moreton and EIT wavefronts for all events with EIT data coverage, except for E9 where Hα is combined with He I. $r_{\mathrm{H}\alpha}(t)$ (*crosses*) and $r_{\mathrm{EIT}}(t)$ (*circles*) are plotted together with 2nd degree polynomial fits (*thick line*) and power-law fits (*thin line*) of the combined distances $r(t)$. For E3, the positions of the X-ray wave (*triangles*) are indicated, too, while for E9, both $r_{\mathrm{H}\alpha}(t)$ and $r_{\mathrm{He\,I}}(t)$ (*diamonds*) are plotted together with 2nd degree polynomial fits of the two data types. For E12, $r_{\mathrm{He\,I}}(t)$ (determined with the "profile" method) is shown together with the fits of the combined Hα and EIT fronts.

We conclude that X-ray waves can also be attributed to the same disturbance that creates the other signatures of flare waves.

5.5. 17 GHz radioheliograms

Due to their diffuse and noisy nature no detailed study of the kinematics of the flare waves visible in the 17 GHz radioheliograms has been carried out. However, as the morphological studies have shown (see Sect. 3.5), the 17 GHz waves are closely associated with Moreton waves, and it is reasonable to assume that their kinematical parameters will be broadly similar, too. Indeed, the $r(t)$ measurements in E6 show that the 17 GHz disturbance follows the same kinematical curve as the Moreton wave, but it seems to lead by ≈20 Mm (note that this value is highly ambiguous due to the low accuracy of the distance measurements).

6. Discussion

Signatures of flare waves were found in five different spectral bands – Hα (line center and wings), EUV, He I, SXR and 17 GHz. It seems that in a flare wave event of sufficient amplitude all signatures are present. The waves in the different channels were found to follow closely associated kinematical curves, which suggests that they are caused by the same physical disturbance. In the case of Hα and EIT waves, the close association is directly evident from the observations of nearly cospatial (and morphologically similar) Hα and EIT wavefronts in E1 and especially in E5 (see Sect. 3.2).

The presented analysis shows that all flare waves are decelerating. This causes an artificial velocity discrepancy between EIT and Hα signatures: the EIT signatures *must* show

Table 4. EIT and combined Hα/EIT wave kinematics. $\bar{v}_{\mathrm{EIT}}$ is the mean EIT velocity, $r_{\mathrm{EIT}}^{\mathrm{min}}$ and $r_{\mathrm{EIT}}^{\mathrm{max}}$ the minimum and maximum EIT distance, $\bar{v}_{cb}$ the mean combined velocity, $\bar{a}_{\mathrm{vb}}$ the mean combined deceleration, and δ_{cb} the exponent of the power-law fits of the combined data.

Event	$\bar{v}_{\mathrm{EIT}}$	$r_{\mathrm{EIT}}^{\mathrm{min}}$	$r_{\mathrm{EIT}}^{\mathrm{max}}$	$\bar{v}_{cb}$	$\bar{a}_{cb}$	δ_{cb}
E1	328	180	855	333	−88	0.78
E2	145	581	727	226	−130	0.47
E3	258	184	524	279	−480	0.52
E4	308	618	933	407	−254	0.61
E5	376	210	889	390	−326	0.61
E10	402	457	746	530	−390	0.69
E11	387	535	813	531	−488	0.62
E12	285	358	796	316	−116	0.72
Mean:	311	390	785	377	−284	0.63
σ:	84	183	126	111	162	0.1

lower mean velocities than their Hα counterparts because they can be traced to much larger distances ($\langle r_{\rm EIT}^{\rm max}\rangle$ = 785 Mm, compared to $\langle r_{\rm H\alpha}^{\rm max}\rangle$ = 301 Mm). For example, the mean Hα wave speed is $\langle \bar{v}_{\rm H\alpha}\rangle$ = 643 km s^{-1}, while the mean EIT wave speed $\langle \bar{v}_{\rm EIT}\rangle$ is just 311 km s^{-1}. The discrepancy is increased furthermore by the low cadence of the EIT observation, resulting in a poor coverage of fast events (i.e. a fast wave is recorded on only one image, which is insufficient for speed estimates).

It should be noted that Eto et al. (2002) conclude that Moreton and EIT waves are not closely related. They studied E4 and found that a small filament far from the AR started oscillating. They concluded that the Moreton wave (assuming constant propagation speed) could well have activated the filament, but the location of the EIT wave was found to be inconsistent with this picture – the EIT wavefront which was observed 2 min after the start of the filament oscillation had not yet reached the filament. While we find this inconsistency to be somewhat smaller than reported in Eto et al. (2002), the oscillation still seems to have been initiated before the EIT wave had reached the filament. This might be due to the fact that the wave is actually inclined to the solar surface (as is the case for the event studied by Hudson et al. 2003), and has already progressed farther at greater heights where the wave is not observable with EIT (at least not on the disk). Since the filament is also extended in height – it was a polar crown filament and their heights are typically several tens of Mm – the interaction with the flare wave could actually be initiated before the parts of the wave that are propagating at the coronal base reach the filament.

Recently, Chen et al. (2002) found from a numerical simulation that an erupting flux rope would generate two distinct waves. A fast wave (a slightly supermagnetosonic shock) would be piston-driven by the expanding CME. This wave is identified with the Moreton wave, and referred to as "coronal Moreton wave". In addition, a slower wavefront would be generated by the successive opening of field lines, producing successive density enhancements. This disturbance (which is not a real wave) would correspond to the EIT wave and trail behind the fast wave at roughly one third of the velocity of the latter. Harra & Sterling (2003) provided some observational evidence for this model using a weak flare wave event.

However, among the class of events we are studying (which all showed initially fairly "sharp" disturbances), we do not find evidence supporting the Chen model. First, we do not observe two distinct wavefronts in any of our wavelength ranges. The two-part structure of the He I disturbances also cannot be interpreted in the framework of the Chen model, since they move basically at the same speeds. Lastly, the EIT wave in the Chen model decelerates much more strongly than the Moreton wave (see Fig. 2 in Chen et al. 2002), which is contrary to what we found (see Sect. 5.2).

Even though we cannot support the conclusions reached by Eto et al. (2002) and Chen et al. (2002), these studies again pose the question if EIT waves *in general* can be attributed to the same class of disturbances as Moreton waves. The average EIT wave speed for the eight events of this study is $\langle \bar{v}_{\rm EIT}\rangle$ = 311 km s^{-1}, while it is slightly lower ($\langle \bar{v}_{\rm EIT}\rangle$ = 271 km s^{-1}) for the 20 events in Klassen et al. (2000), and much lower ($\langle \bar{v}_{\rm EIT}\rangle$ = 189 km s^{-1}) for the 176 events in studied by Myers & Thompson (Thompson, private communications). Based on these velocities, we can conclude that the EIT waves of Klassen et al. (2000) belong to the same class of events as the EIT waves presented in this study. The sample of Myers & Thompson, on the other hand, contains many events with speeds of just several tens of km s^{-1}, i.e. one order of magnitude lower than the characteristic speeds of flare waves. It is therefore probable that this sample contains EIT disturbances that are not really waves at all, but which are generated by a totally different physical process than the "real" EIT waves which are produced by the same disturbance that causes the flare waves in the other spectral channels. Hence, we conclude that at least the EIT waves in our sample are caused by the same disturbance that creates the Moreton waves and the other signatures of flare waves in additional spectral channels.

The He I waves have kinematical parameters that lie in between the values for Hα and EIT waves, and can thus be regarded as a "missing link" between Moreton and EIT waves, which further strengthens the argument that all signatures of flare waves are caused by a common agent. However, the He I signatures lead the Moreton fronts by 20−40 Mm. Therefore some agent must be present that creates the observed He I signatures even before the shock arrives at a given point of the chromosphere (see Vršnak et al. 2002). This could be also related to the "premature" activation of the filament in E4.

In the events with X-ray and radioheliographic flare waves, the disturbances are found to be closely associated with the Moreton waves. They follow basically the same kinematical curves, and are either cospatial with the Moreton fronts, or are slightly ahead of them (by 10−20 Mm).

7. Conclusion

12 Hα Moreton wave events have been studied. For these events, wave signatures were also detected in EIT Fe XII images, in He I filtergrams, in *Yohkoh*/SXT images, and in 17 GHz radioheliograms, and it seems that in an event of sufficient amplitude all of these signatures will be present. In Hα, it was evident that the signatures were created by an enhancement of pre-existing chromospheric structures, and at all wavelengths the leading edges of the wavefronts showed good agreement with a circular fit. These results confirm the wave-like nature of the disturbances, and rule out scenarios in which the wavefronts are directly created by propagating matter (e.g. ejected material impacting on the chromosphere) or other non-wave agents.

The flare waves seen in the different spectral channels all follow closely associated kinematical curves, which implies that they are caused by a common physical disturbance. This notion is supported by morphological similarities between the different signatures. Furthermore, it was found that the waves do not propagate with constant velocities, instead, all flare waves are decelerating. This confirms the results obtained by Warmuth et al. (2001) and Vršnak et al. (2002). The deceleration rate becomes smaller with increasing distance from their source point.

It was shown that there is no "velocity discrepancy" between Moreton and EIT waves. The differences in the measured speeds can be explained by the deceleration of the disturbance, combined with the fact that its signatures can be traced to much larger distances in EIT than in Hα, and with the low image cadence of EIT.

The main aim of this paper has been the establishment of the basic properties of the flare waves observed in the different spectral bands – their morphology, their spatial characteristics and their kinematics. In Paper II (Warmuth et al. 2004), we will combine these results with studies of the perturbation characteristics and the associated metric type II radio bursts to derive a consistent physical interpretation of the flare wave phenomenon.

Acknowledgements. The work of A.W. was supported by DLR under grant No. 50 QL 0001. Hα data are used with permission of BBSO, New Jersey Institute of Technology, and we thank the BBSO staff for their kind support. We are very grateful to H. Kurokawa and K. Shibata for the provision of Hα data from Hida Observatory. He I data were provided by the High Altitude Observatory of the National Center for Atmospheric Research, which is sponsored by the National Science Foundation, and we thank T. Holzer, H. Gilbert and A. Stanger for their support. Radioheliograms from the Nobeyama Radio Observatory were kindly provided by K. Shibasaki. We thank B. J. Thompson for the provision of Hα data, A. Vourlidas for corrected EIT times, and G. Mann, H. Aurass, and A. Klassen for helpful discussions. *SOHO* is a project of international cooperation between ESA and NASA. *Yohkoh* is a mission of the Institute of Space and Astronautical Sciences (Japan), with participation from the US (NASA) and UK (PPARC). A.W. and A.H. acknowledge the support of the Austrian FWF Project P13653-PHY.

References

Andretta, V., & Jones, H. P. 1997, ApJ, 489, 375
Athay, R. G., & Moreton, G. E. 1961, AJ, 133, 935
Becker, U. 1958, Z. Astrophys., 44, 243
Biesecker, D. A., & Thompson, B. J. 2000, J. Atmos. and Sol.-Terr. Phys., 62, 1449
Biesecker, D. A., Myers, D. C., Thompson, B. J., Hammer, D. M., & Vourlidas, A. 2002, ApJ, 569, 1009
Cliver, E. W., Webb, D. F., & Howard, R. A. 1999, Sol. Phys., 187, 89
Chen, P. F., Wu, S. T., Shibata, K., & Fang, C. 2002, ApJ, 572, L99
Delaboudinière, J.-P., Artzner, G. E., Brunaud, J., et al. 1995, Sol. Phys., 162, 291
Denker, C., Johannesson, A., Marquette, W., et al. 1999, Sol. Phys., 184, 87
Dodson, H. W. 1949, ApJ, 110, 382
Eto, S., Isobe, H., Narukage, N., et al. 2002, PASJ, 54, 481
Gilbert, H. R., Thompson, B. J., Holzer, T. E., & Burkepile, J. T. 2001, AGU Fall Meeting 2001, abstract SH12B-0746
Gopalswamy, N., & Thompson, B. J. 2000, J. Atmos. and Sol.-Terr. Phys., 62, 1457
Harra, L. K., & Sterling, A. C. 2003, ApJ, 587, 429
Harrison, R. A., Bryans, P., Simnett, G. M., & Lyons, M. 2003, A&A, 400, 1071
Harvey, K. L., Martin, S. F., & Riddle, A. C. 1974, Sol. Phys., 36, 151
Hudson, H. S., Khan, J. I., Lemen, J. R., Nitta, N. V., & Uchida, Y. 2003, Sol. Phys., 212, 121
Kerdraon, A., & Delouis, J.-M. 1997, in Coronal Physics from Radio and Space Observations, ed. G. Trottet (Berlin: Springer), Lect. Notes Phys., 483, 192
Khan, J. I., & Hudson, H. S. 2000, GRL, 27, 1083
Khan, J. I., & Aurass, H. 2002, A&A, 383, 1018
Klassen, A., Aurass, H., Mann, G., & Thompson, B. J. 2000, A&AS, 141, 357
Kurokawa, H., Ishiura, K., Kimura, G., et al. 1995, J. Geomag Geoelecter, 47, 1043
MacQueen, R. M., Blankner, J. G., Elmore, D. F., Lecinski, A. R., & White, O. R. 1998, Sol. Phys., 182, 97
Messerotti, M., Otruba, W., Warmuth, A., et al. 1999, in Proc. ESA Workshop on Space Weather, ed. N. Crosby, ESA WPP-155, 321
Moreton, G. E. 1960, AJ, 65, 494
Moreton, G. E., & Ramsey, H. E. 1960, PASP, 72, 357
Moreton, G. E. 1964, AJ, 69, 145
Nakajima, H., Nishio, M., Enome, S., et al. 1994, Proc. IEEE, 82, 705
Narukage, N., Hudson, H. S., Morimoto, T., et al. 2002, ApJ, 572, L109
Nelson, G. S., & Melrose, D. B. 1985, in Solar Radiophysics, ed. D. J. McLean, & N. R. Labrum (Cambridge: Cambridge Univ. Press), 333
Pinter, S. 1977, Spec. Rep. AFGL-SR-209, Hanscom Air Force Base, 35
Pohjolainen, S., Maia, D., Pick, M., et al. 2001, ApJ, 556, 421
Ramsey, H. E., & Smith, S. F. 1966, AJ, 71, 197
Shibata, K., Eto, S., Narukage, N., et al. 2002, in Proc. Yohkoh 10th Anniversary Meeting, ed. P. Martens, Cospar Colloq., 13, 279
Smith, S. F., & Harvey, K. L. 1971, in Physics of the Solar Corona, ed. C. J. Macris (Dordrecht: Reidel), 156
Thompson, B. J., Plunkett, S. P., Gurman, J. B., et al. 1998, Geophys. Res. Lett., 25, 2465
Thompson, B. J., Gurman, J. B., Neupert, W. M., et al. 1999, ApJ, 517, L151
Thompson, B. J., Reynolds, B., Aurass, H., et al. 2000, Sol. Phys., 193, 161
Tsuneta, S., Acton, L., Bruner, M., et al. 1991, Sol. Phys., 136, 37
Uchida, Y. 1960, PASJ, 12, 676
Uchida, Y. 1968, Sol. Phys., 4, 30
Uchida, Y. 1970, PASJ, 22, 341
Uchida, Y., Altschuler, M. D., & Newkirk, G., Jr. 1973, Sol. Phys., 28, 495
Uchida, Y. 1974, Sol. Phys., 39, 431
Valniček, B. 1964, Bull. Astron. Inst. Czech., 15, 207
Vršnak, B., & Lulić., S. 2000a, Sol. Phys., 196, 157
Vršnak, B., & Lulić., S. 2000b, Sol. Phys., 196, 181
Vršnak, B., Warmuth, A., Brajša, R., & Hanslmeier, A. 2002, A&A, 394, 299
Warmuth, A., Vršnak, B., Aurass, H., & Hanslmeier, A. 2001, ApJ, 560, L105
Warmuth, A., Vršnak, B., Magdalenić, J., Hanslmeier, A., & Otruba, W. 2004, A&A, 418, 1117